

Crystal structure and physical properties of Ba₂Nb₃S₈I: A new misfit-layered transition-metal dichalcogenide superconductor

M.G. Smith^a, Qisheng Lin^b, S.M. Benjamin^a, Mitchell T. Baker^a, J.J. Neumeier^{a,*}

^a Physics Department, Montana State University, Bozeman, MT, 59717-3840, USA

^b Ames Laboratory, Department of Chemistry, Iowa State University, 2416 Pammel Dr., Ames, IA, 50011-2416, USA

ARTICLE INFO

Keywords:

Single crystal growth
Vapor transport
Electrical resistivity
Superconductivity

PACS:

74.10.+v
74.25.Bt
74.70.Xa

ABSTRACT

Single crystals of Ba₂Nb₃S₈I have been grown using iodine-vapor transport in fused-quartz tubes. The crystals form as flakes with typical areas of 5–10 mm² and thicknesses of 5–11 μm. The crystal structure was determined using single-crystal x-ray diffraction with the aid of an APEX II CCD diffractometer. The structure shows trigonal symmetry with space group *P31c* and lattice parameters $a = b = 10.0156(5)$ Å and $c = 25.1414(15)$ Å. Compositional analysis via x-ray spectroscopy confirms the presence of iodine. Superlattice reflections are evident in x-ray precession images. Measurements of the electrical resistivity reveal a metallic temperature dependence and superconductivity near 1 K. Polycrystalline samples of Ba₂Nb₃S₈I were made in order to have samples large enough for other bulk physical properties measurements. Magnetic susceptibility reveals antiferromagnetism below 275 K. The coexistence of antiferromagnetism and superconductivity is surprising. Specific heat measurements reveal the electronic coefficient $\gamma = 3.95(66)$ mJ/mol K². The jump in the specific heat at the superconducting transition temperature T_c ($\Delta C/\gamma T_c = 1.4(2)$) and the energy gap associated with the superconducting state ($E_g = 0.405(17)$ meV) agree well with BCS theory.

1. Introduction

The layered transition metal dichalcogenides (TMD) have a hexagonal structure in which a layer of metal atoms is covalently bonded to, and sandwiched between, two layers of chalcogens (X-M-X, X = S, Se and Te; M = Group IV to VII transition metals). The X-M-X layers are bonded together by weak van der Waals forces, which permit intercalation of atoms, ions, and inorganic and organic molecules between the layers [1]. Intercalation can result in the so-called misfit-layer compounds (MS)_xTS₂. (M = transition metals, Sn, Pb, Bi, rare earth metals; T = Nb, Ta; x = 0.6 and 1.2) if the intercalant consists of a slab with strong covalent bonding between the atoms [2]. The x = 1.2 compounds have one MS layer and one TS₂ layer alternately stacked along the c-axis (a Stage-1 compound) [3]. The x = 0.6 compounds have one MS layer stacked between two TS₂ layers along the c-axis (a Stage-2 compound). Recent work has shown stresses between adjacent layers due to lattice periodicity mismatch in (MS)_xTS₂ compounds provide a driving force for curling of the layers and the elimination of dangling bonds [4]. The combination of both can result in the formation of misfit-layered nanotubes by single-crystal vapor-transport and laser-ablation

synthesis methods [4].

NbS₂, the host dichalcogenide of many misfit-layer (MS)_xTS₂ compounds, occurs in four phases [5]. They are stoichiometric 2H-NbS₂ and 3R-NbS₂ and non-stoichiometric 2H-Nb_{1+x}S₂ and 3R-Nb_{1+x}S₂. The stoichiometry of the product phase depends on sulfur pressure; x decreases with increasing pressure [6]. Bulk superconductivity occurs in 2H-NbS₂ at $T_c = 6.3$ K and in 2H-Nb_{1+x}S₂ at $T_c = 6.04$ – 6.3 K for $0.001 \leq x \leq 0.029$ [6,7]. Intercalation of transition metals M into host TX₂ compounds to form M_xTX₂ (x < 1.0) generally results in layered structures for Group IV–VII metals, and non-layered structures for some of the Group VIII–X metals with changes in electrical and magnetic properties [8]. In the particular case of M_xNbS₂ with M = Cu, T_c and the superconducting volume fraction are reduced for x < 0.6 and superconductivity disappears for x > 0.6 [1]. Cr_{0.33}NbS₂ is a metallic ferromagnet [9] below ~160 K, whereas Fe_{0.33}NbS₂ orders antiferromagnetically [10] below 137 K.

Intercalation of more complex MS layers into TS₂ to form misfit-layered (MS)_xTS₂ compounds also results in a diverse range of electronic properties including semiconducting, and metallic behaviors, thermoelectricity, superconductivity, ferromagnetism, and

* Corresponding author.

E-mail address: neumeier@montana.edu (J.J. Neumeier).

<https://doi.org/10.1016/j.jpcs.2021.110135>

Received 10 August 2020; Received in revised form 10 November 2020; Accepted 29 April 2021

Available online 18 May 2021

0022-3697/© 2021 Elsevier Ltd. All rights reserved.

antiferromagnetism, depending on the nature of the intercalant and whether they are Stage-1 or Stage-2 compounds [2,11,12]. For example, $(\text{LaS})_{1.14}\text{TS}_2$ is a high-temperature thermoelectric material with a figure-of-merit $ZT \sim 0.14$ near 950 K [13,14]. Bulk superconductivity at $T_c = 3$ K occurs in $(\text{MS})_{1.2}\text{TS}_2$ ($M = \text{Sn, Pb}$ and $T = \text{Nb, Ta}$) and at $T_c = 0.8$ K in $(\text{BiS})_{1.2}\text{TaS}_2$ [15]. $(\text{CeS})_{1.2}\text{NbS}_2$, $(\text{GdS})_{1.2}\text{NbS}_2$, and $(\text{CeS})_{0.6}\text{NbS}_2$ order antiferromagnetically at 3.2 K, 4.6 K, and 3.0 K, respectively [11,16,17].

In the course of attempting to grow crystals of the $T_c = 0.85$ K superconductor BaNb_2S_5 via iodine-vapor transport [18] we grew foil-like crystals of a new superconducting misfit-layered TMD with stoichiometry $\text{Ba}_2\text{Nb}_3\text{S}_8\text{I}$. Many of the crystals were curled at their edges. With its distorted layer of salt-like BaS containing interstitial iodine atoms, $\text{Ba}_2\text{Nb}_3\text{S}_8\text{I}$ is a new addition to the rich family of intercalated TMDs. Single-crystal x-ray diffraction reveals a trigonal crystal structure with $P31c$ space group. The intercalated salt-like BaS layer is distorted from rocksalt BaS (lattice parameter $a = 6.386$ Å) because of lattice mismatch with the NbS_2 host (lattice parameter $a = 3.33$ Å) layer; pure BaS is a wide-gap semiconductor [19]. The distortion from cubic symmetry in the BaS layer allows incorporation of iodine into the hexagonal tunnels of the layer. $\text{Ba}_2\text{Nb}_3\text{S}_8\text{I}$ can be viewed as a Stage-1 compound, since the BaS and NbS_2 layers alternate along the c crystallographic direction.

In this report we describe crystal growth and crystal-structure determination of single-crystalline $\text{Ba}_2\text{Nb}_3\text{S}_8\text{I}$. Polycrystalline specimens of the same composition were made in order to have samples large enough for a host of bulk physical properties measurements. Electrical resistivity, magnetic susceptibility, specific heat, and Hall effect measurements reveal that $\text{Ba}_2\text{Nb}_3\text{S}_8\text{I}$ is a metal that exhibits bulk superconductivity in the vicinity of 1 K.

2. Experimental methods

Two methods were used to grow single crystalline samples of $\text{Ba}_2\text{Nb}_3\text{S}_8\text{I}$. For the first sample, referred to as Sample A, BaS was synthesized by placing BaCO_3 in an alumina crucible, which was inserted into a quartz tube in a tube furnace. The tube furnace was contained in a fume hood to exhaust CS_2 fumes [20] from the laboratory. Nitrogen gas was passed through a pumice stone submerged in CS_2 ; the resulting gas was then passed through the quartz tube. The sample was reacted in this environment at 800 °C for 12 h, reground, and reacted in the CS_2 -laden gas a second time at 800 °C for 15 h. The resulting BaS was combined with Nb Powder (99.99% purity), and S (USP purity) in the stoichiometry BaNb_2S_5 , mixed using a mortar for approximately 1.5 min, and then placed in a fused quartz tube with 14 mm i.d. that was 13 cm in length. A sufficient mass of iodine was added to the tube to reach a maximum pressure of 1 atm at the highest reaction temperature to promote vapor transport. The tube was evacuated and flushed three times with nitrogen gas and then sealed. The tube was then heated to 500 °C in 5 h, held there for 2 h, heated to 950 °C in 6 h, held there for 250 h, and slow cooled over 24 h to room temperature. A gradient of about 11.5 °C/cm was maintained across the tube by positioning the hot end at 950 °C and the cooler end at 800 °C in the tube furnace. For the second sample, referred to as Sample B, a BaNb_2S_5 polycrystalline sample was produced by mixing stoichiometric amounts of Ba metal (99.27% purity), Nb powder (99.99% purity), and S (USP purity). Two pieces of Ba metal were cut from a larger piece in a nitrogen glove box and sanded to remove any surface contaminants. Nb powder was then mixed with sulfur outside of the glovebox using a mortar and pestle. The Ba metal and Nb-S powder mixture were placed in an alumina boat, which was placed inside of a 14 mm i.d. quartz tube, 16 cm in length, along with sufficient iodine to provide one atm of pressure at the maximum reaction

temperature. The tube was evacuated and flushed with nitrogen three times and then sealed. The tube was then heated in 6 h to 650 °C, held there for 1 h, heated in 6 h–1000 °C, held there for 24 h, cooled over 48 h to 800 °C, held at 800 °C for 48 h, and cooled over 12 h to room temperature. Several unsuccessful attempts were also made to grow crystals using Cl as the transport medium by adding TeCl_4 to the quartz tube instead of iodine.

After the stoichiometry and crystal structure of the single crystals were determined (see Section 3.1), bulk samples of $\text{Ba}_2\text{Nb}_3\text{S}_8\text{I}$ were synthesized in order to measure the bulk physical properties, since the single crystals, flake-like in morphology, do not possess enough mass for most physical properties measurements. Two different synthesis routes were used. BaS and NbS_2 were first synthesized using BaCO_3 and Nb powder in alumina boats heated at 800 °C and 900 °C, respectively, in flowing CS_2 . X-ray diffraction confirmed the desired materials were obtained. One $\text{Ba}_2\text{Nb}_3\text{S}_8\text{I}$ sample was synthesized with stoichiometric amounts of BaS, Nb and S powders. The second sample was synthesized with stoichiometric amounts BaS and NbS_2 powders. We note that there is an excess of S in this preparation method. Both samples were then given the following treatment. The powders were mixed using a mortar and pestle for 5 min before placement in a quartz tube. Sufficient crystalline I_2 was added to achieve a pressure of 1 atm at 800 °C within the sealed tube. The tube was flushed three times with N_2 , and sealed when the pressure reached 5.0×10^{-2} mbar. The tube was then heated to 500 °C over 5 h, held there for 2 h, heated to 800 °C over 6 h, held there for 24 h, and slow-cooled to room temperature over 12 h. The resultant black powder was ground using a mortar and pestle for 5 min, pressed into a pellet, and placed in a quartz tube. Sufficient crystalline I_2 was added to the tube to achieve a pressure of 1 atm at 800 °C within the tube. The tube was flushed three times with N_2 , and sealed when the pressure fell below 5.0×10^{-2} mbar. It was then heated to 500 °C over 2 h, held there for 1 h, heated to 800 °C over 3 h, held there for 24 h, and slow-cooled to room temperature over 12 h. Typical densities of the polycrystalline samples were 3.26(4) g/cm³, which is approximately 76% theoretical density.

A photograph of typical crystals is shown in Fig. 1. They are 1–7 mm in length, on edge, and a scanning-electron microscope was used to measure the thickness of some, yielding values ranging from 5 to 11 μm. Measurements taken on the $\text{Ba}_2\text{Nb}_3\text{S}_8\text{I}$ crystals are noted here. Several powder x-ray diffraction patterns (XRD) were acquired from pulverized single crystals. The XRD data of Sample B sample yielded the following lattice parameters through a method of cell refinement using the space group $P31c$: $a = 9.9958(18)$ Å, $c = 25.0680(30)$ Å, and $V = 2169$ Å³. These values agrees with the lattice parameters determined for the single crystals by x-ray diffraction (see Section 3.1): $a = 10.016(5)$ Å, $c = 25.1414(15)$ Å, $V = 2184.1(15)$ Å³. The electrical resistivity was measured using a Quantum Design Physical Properties Measurement System (PPMS); the uncertainty is about 30%, which is associated with the uncertainty in the thickness of the measured single crystal.

Additional measurements were carried out using the PPMS on the bulk polycrystalline specimens. Electrical resistivity was measured with a four-probe dc method using current densities of about 3.5 A/cm²; when magnetic field was present, the field was perpendicular to the current direction. The Hall effect was measured in order to determine the net charge-carrier density. For these measurements, a current density of 1.3 A/cm² was applied to the sample at an excitation frequency of 17 Hz; the transverse voltage was balanced in zero magnetic field using three voltage taps and the Hall voltage was determined using an 8 T magnetic field for both field directions to further correct for any remaining transverse voltage *not* associated with the Hall effect. Magnetic susceptibility data was acquired using a vibrating sample

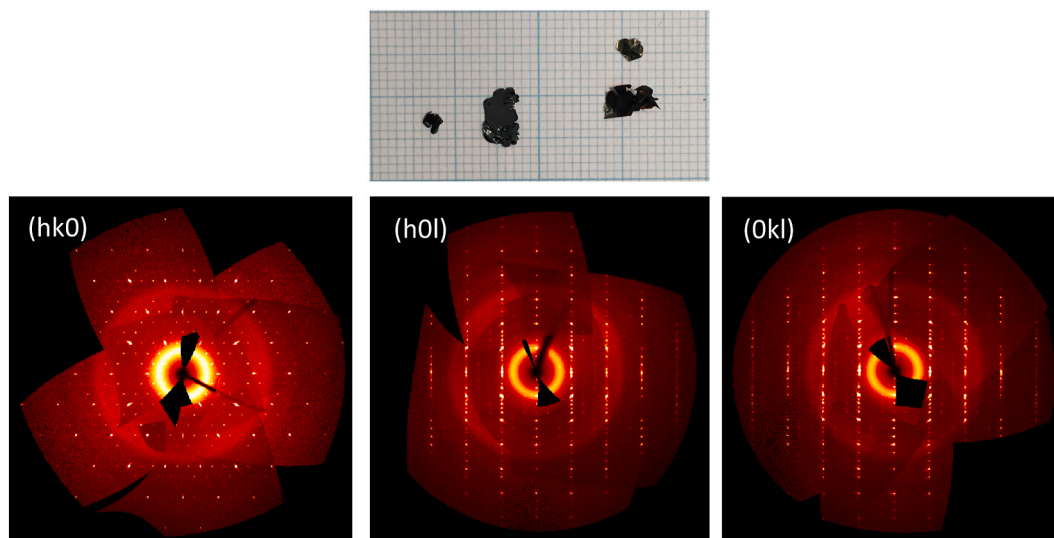


Fig. 1. (Top Row) Optical image of selected single crystals of $\text{Ba}_2\text{Nb}_3\text{S}_8\text{I}$; the dimensions of the small squares are $1 \text{ mm} \times 1 \text{ mm}$. Thicknesses of the crystals are $5\text{--}11 \mu\text{m}$. (Bottom Row) X-ray precession images for single-crystalline $\text{Ba}_2\text{Nb}_3\text{S}_8\text{I}$ projected along axial directions. Weak diffraction spots along $(0kl)$ and $(h0l)$ denote 3 times superlattice in a and b compared with the base structure of TMD (e.g., $\sim 3.3 \text{ \AA}$ for NbS_2). Note some diffraction spots are elongated, a signature of disorder in the structure.

magnetometer in a magnetic field of 2 T. A small amount of Duco® cement, thinned with 40% acetone by volume, was used to fasten the sample to the VSM paddle. Specific heat was measured using a standard heat-pulse method.

3. Results

3.1. Structure determination

Single crystal X-ray diffraction data were collected at 293 K using a Bruker SMART APEX II diffractometer (Mo $K\alpha$ radiation, $\lambda = 0.71073 \text{ \AA}$). Mixed ω and φ scan modes were used over 2θ ranges of 3° to 68° , with duration of exposure set at 30 s per frame. Data reduction, integration, unit-cell refinements, and absorption corrections were accomplished with the aid of the APEX3 software package [21], which suggested trigonal symmetry with $a = b = 10.0156(5) \text{ \AA}$ and $c = 25.1414(15) \text{ \AA}$. The processed data were imported to Jana2006 [22]. A space group of $P31c$ was suggested by the program SUPERFLIP [23], together with an initial model with all 16 independent crystallographic sites, including Ba, Nb, and S atoms and one I atom assigned to the I5 site. Assignments of Ba, Nb and S atoms are quite straightforward based on electron density and inter-atomic distances. However, the I5 site is abnormal if assigned to Ba (its separation is too short from its neighbors), Nb (too large displacement parameter and too large separation from neighboring atoms), or S (large displacement parameters, large separation from neighboring atoms, and homoatomic neighbors). Considering the electron density and interatomic distance, iodine was favorably assigned to this site. Energy Dispersive X-Ray Spectroscopy (EDAX) analysis confirms the presence of iodine (see Section 3.2). All these suggest the introduction of the element iodine from the transport agent. Subsequent difference Fourier map and distance analyses revealed all remaining I atoms with partial occupancies. Considering the short distances for I1–I2 (1.73 \AA) and I3–I4 (2.21 \AA) pairs, the sum occupancy for each pair was fixed to unity to be reasonable in crystallography. In other words, each I1/I2 and I3/I4 pair is actually one iodine atom with split position. In contrast, the split of I5 atoms are much smaller, with 4% electron density deviating about 0.8 \AA . Therefore, the I5 atom was not refined with split position, it thus exhibits the largest isotropic displacement parameter (0.194 \AA^2). The disorder feature can be traced by the elongated x-ray diffraction spots in the precession images projected along

Table 1

Crystal data and structure refinement for $\text{Ba}_2\text{Nb}_3\text{S}_8\text{I}$.

Empirical Formula	$\text{Ba}_2\text{Nb}_3\text{S}_8\text{I}$
Formula weight	936.8
Space group	$P31c$
Unit cell dimensions	$a = b = 10.0156(5) \text{ \AA}$ $c = 25.1414(15) \text{ \AA}$
Unit cell volume	$2184.1(15) \text{ \AA}^3$
Z	6
Density (calculated)	4.2733 g/cm^3
Absorption coefficient	10.845 mm^{-1}
Reflections collected	36711 [R(int) = 0.1578]
Data/restraints/parameters	5439/0/101
Goodness-of-fit on F^2	1.04
Final R indices [$I > 2\sigma(I)$]	$R1 = 0.0585$, $wR2 = 0.1117$
R indices (all data)	$R1 = 0.2092$, $wR2 = 0.1619$
Largest diff. peak and hole	5.10 and -4.57 e.\AA^{-3}

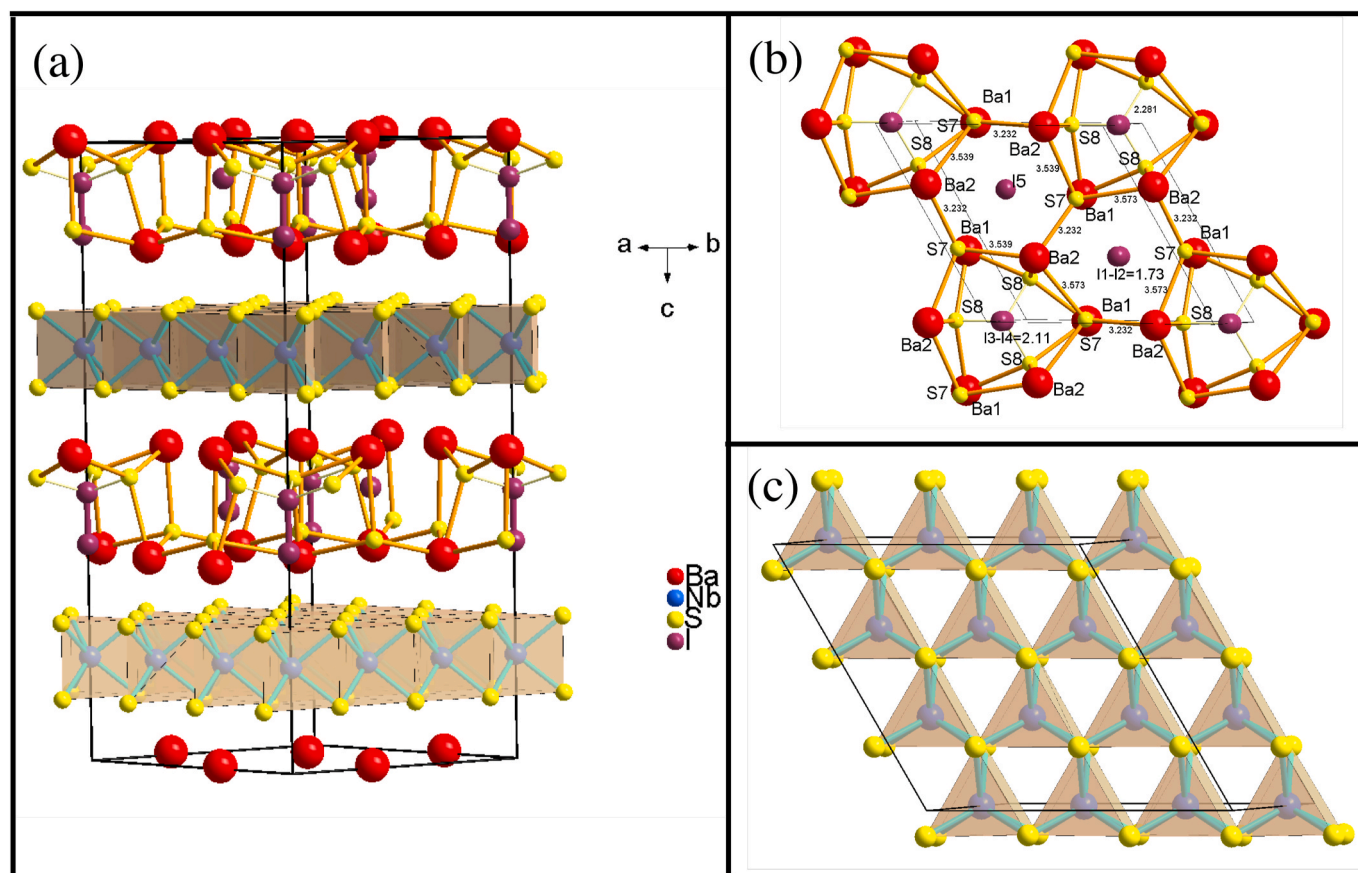
axial directions, see Fig. 1. The final least square refinement on F^2 converged at $R1 = 5.85\%$ and $wR2 = 11.17\%$ for reflections $I > 3(\sigma)I$ and a formula of $\text{Ba}_2\text{Nb}_3\text{S}_8\text{I}$. The final model was further checked with the program Platon [24]; no higher symmetry than the acentric space group $P31c$ was suggested. Table 1 gives the detailed crystal data and structure refinements for this new compound, and Table 2 lists the refined atomic parameters, Wyckoff sites, site symmetry and occupancy, and isotropic displacement parameters.

The structure of $\text{Ba}_2\text{Nb}_3\text{S}_8\text{I}$ is a $3 \times 3 \times 2$ superstructure of the base material 2H-NbS_2 ($a = b = 3.32 \text{ \AA}$, $c = 11.97 \text{ \AA}$). The formula can be written as $(\text{NbS}_2)(\text{BaS})_{0.67}(\text{I})_{0.33}$, to better represent its structural motifs. That is, the structure features two-dimensional (2D) $[\text{NbS}_2]_\infty$ layers consisting of interlinked NbS_6 trigonal prisms, as shown in Fig. 2 (a) and (c). Sandwiched between neighboring $[\text{NbS}_2]_\infty$ layers are salt-like layers with dominant composition of BaS as shown in Fig. 2(a) and (b), together with the interstitial iodine atoms incorporated from the transport agent used in the crystal growth. Atoms involved in the 2D layer include all Nb atoms and the S1 through S6 atoms as illustrated in Fig. 2(c). The 2D nature is common for transition metal sulfides. It is worthy to note that the isotropic displacement parameters for atoms in the BaS layer ($> 0.026 \text{ \AA}^2$) are at least two times larger than those in the $[\text{NbS}_2]_\infty$ layers ($\sim 0.012 \text{ \AA}^2$). This is attributed to the disordered nature of the iodine atoms located in the hexagonal tunnels of the BaS layer.

Table 2

Atomic coordinates and equivalent isotropic displacement parameters for $\text{Ba}_2\text{Nb}_3\text{S}_8\text{I}$. U_{eq} is defined as one third of the trace of the orthogonalized U^{ij} tensor.

Atom	Wyck	Symm.	occupancy	x	Y	z	U_{eq} (\AA^2)
Ba1	6c	1	1	-0.3518(2)	0.6455(2)	0.4950(5)	0.036(1)
Ba2	6c	1	1	-0.0125(2)	0.6772(2)	0.1654(5)	0.039(1)
Nb1	6c	1	1	0.0000(2)	0.6673(2)	0.3305(5)	0.013(1)
Nb2	2a	3..	1	0	0	0.3315(5)	0.011(1)
Nb3	6c	1	1	0.3343(2)	0.9992(2)	0.3302(5)	0.012(1)
Nb4	2b	3..	1	-1/3	1/3	0.3297(6)	0.012(1)
Nb5	2b	3..	1	1/3	2/3	0.3304(5)	0.012(1)
S1	6c	1	1	-0.2232(5)	0.5563(5)	0.2700(6)	0.012(1)
S2	6c	1	1	0.1096(5)	0.5527(5)	0.2692(6)	0.012(1)
S3	6c	1	1	0.1138(5)	0.8917(5)	0.2703(6)	0.012(1)
S4	6c	1	1	-0.2237(5)	0.5543(5)	0.3935(6)	0.012(1)
S5	6c	1	1	0.1132(5)	0.5571(5)	0.3932(6)	0.012(1)
S6	6c	1	1	0.1142(5)	0.8911(5)	0.3940(6)	0.012(1)
S7	6c	1	1	-0.3766(5)	0.6355(5)	0.1352(6)	0.026(1)
S8	6c	1	1	0.0016(6)	0.7835(4)	0.5375(6)	0.026(1)
I1	2b	3..	0.448(6)	-2/3	2/3	0.0967(6)	0.083(2)
I2	2b	3..	0.552(6)	-2/3	2/3	0.0270(8)	0.083(2)
I3	2a	3..	0.212(5)	0	0	0.6486(7)	0.030(1)
I4	2a	3..	0.788(5)	0	0	0.5646(6)	0.030(1)
I5	2b	3..	1	-1/3	1/3	0.0605(9)	0.194(4)

Fig. 2. (a) Unit cell of $\text{Ba}_2\text{Nb}_3\text{S}_8\text{I}$. (b) BaS layers (c) NbS_2 layers.

The program JADE (version 9.5.0) was used to calculate the theoretical x-ray powder pattern for $5^\circ \leq 2\theta \leq 70^\circ$ using the obtained crystallographic data (Tables 1 and 2). The calculated hkl , 2θ values, and intensities for selected reflections are shown in Table 3. Jade was used to conduct a peak search of the measured x-ray powder pattern for the polycrystalline specimens, and a least-square refinement of the 2θ positions and lattice constants. It provides estimated 2θ standard deviation values and the Smith-Snyder Figure of Merit, FN, an alternative method for evaluating the fit quality in x-ray powder diffraction pattern analysis

[25]. For the polycrystalline sample of the first synthesis (BaS + Nb + S), 26 peaks were fit in the two-theta range $5-70^\circ$ to the $P31c$ unit cell, obtaining lattice parameters $a = 10.017(2) \text{ \AA}$, $c = 25.255(5) \text{ \AA}$, and a unit-cell volume of 2194.60 \AA^3 (FN = 4.9 and 2θ standard deviation of 0.025°), in good agreement with the single-crystal results. The indexed x-ray powder pattern is shown in Fig. 3. Observed hkl values, 2θ values, and intensities (relative to the 306 reflection) of the fitted reflections are given in Table 3. Similar results were obtained for the polycrystalline sample from the second synthesis (BaS + NbS_2). A small unidentified

Table 3

Calculated and observed reflections and intensities for x-ray powder diffraction pattern of the polycrystalline $\text{Ba}_2\text{Nb}_3\text{S}_8\text{I}$ specimen.

hkl	Calculated 2θ	Calculated Intensity	Observed 2θ	Observed Intensity
0 0 2	7.026	64.2	7.058	9.9
0 0 4	14.079	44.2	14.078	21.1
0 0 6	21.186	32.4	21.063	10.2
2 1 0	27.176	5.4	27.176	8.8
2 1 1	27.411	0.5	27.528	4.9
1 0 8	30.223	1.0	29.933	10.5
3 0 0	30.900	95.3	30.901	93.5
3 0 4	34.104	24.6	34.081	21.6
2 2 2	36.559	12.8	36.180	10.5
3 0 6	37.770	100	37.705	100
3 0 8	42.446	18.2	42.342	12.1
3 1 6	43.332	1.6	43.304	3.3
3 0 9	45.090	4.6	44.931	3.2
3 2 2	46.144	0.7	45.958	1.4
3 0 10	47.908	8.0	47.778	11.6
3 0 12	54.055	31.0	53.821	11.5
5 0 3	53.925	0.10	53.898	11.7
3 3 0	54.957	34.4	54.901	23.9
3 3 2	54.481	3.7	55.429	7.8
4 0 10	55.949	0.8	55.855	2.8
3 3 6	59.562	8.6	59.501	8.1
6 0 0	64.389	9.1	64.306	7.7
6 0 1	64.508	1.6	64.521	4.5
0 0 18	66.939	3.9	66.639	3.2
5 2 3	68.405	0	68.441	17.5
6 0 6	68.613	13.0	68.552	10.6

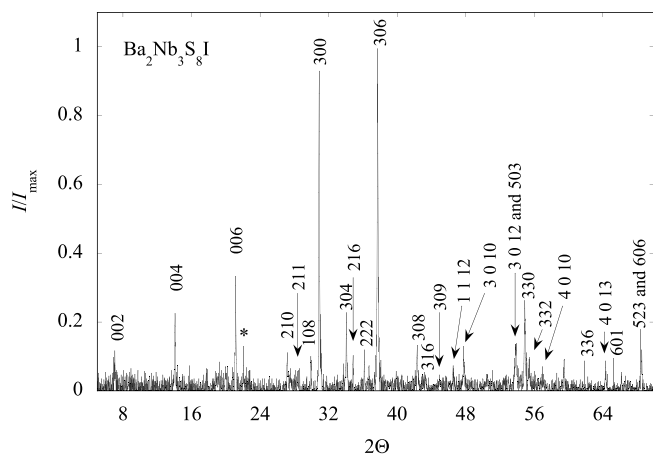


Fig. 3. X-ray diffraction pattern for polycrystalline $\text{Ba}_2\text{Nb}_3\text{S}_8\text{I}$. The peaks are indexed to the $P31c$ unit cell. Impurity peaks are labeled with *.

impurity was observed at $2\theta = 22.079^\circ$ in both samples. In the supplementary information accompanying this communication, Figure S1 compares the x-ray patterns of $\text{Ba}_2\text{Nb}_3\text{S}_8\text{I}$, BaNb_2S_5 , and BaNbS_3 .

In order to determine if iodine is necessary to intercalate a rocksalt-like BaS layer between NbS_2 layers, we attempted to synthesize “ $\text{Ba}_2\text{Nb}_3\text{S}_8$ ” following a procedure similar to that used to synthesize polycrystalline $\text{Ba}_2\text{Nb}_3\text{S}_8\text{I}$, by placing stoichiometric amounts of BaS, Nb and S in an evacuated quartz tube *without* iodine. If “ $\text{Ba}_2\text{Nb}_3\text{S}_8$ ” were to form in the same structural type, the powder pattern would be similar, with peak positions shifted to higher angles due to smaller lattice parameters. X-ray diffraction revealed a mixture of BaS and an unidentified phase. There was no evidence of a “ $\text{Ba}_2\text{Nb}_3\text{S}_8$ ” phase in our sample. The x-ray data for this sample is compared to that of $\text{Ba}_2\text{Nb}_3\text{S}_8\text{I}$ in Figure S2 in the supplementary information accompanying this paper. We conclude that iodine is needed to stabilize the rocksalt-like BaS layer between NbS_2 layers, and in turn, to stabilize $\text{Ba}_2\text{Nb}_3\text{S}_8\text{I}$. Intercalation of I^- with its large radius of 220 pm [26] most likely stabilizes the

distortion from cubic symmetry of the BaS layer and permits its incorporation between the NbS_6 trigonal prism layers of NbS_2 . In contrast, a smaller ion like Cl^- is not favorable here, as confirmed by our experiments (see Section 2). For intercalated $(\text{MS})_x(\text{TS}_2)$ TMD compounds, the value of x is commonly found to be ≤ 1.2 . In our case, $x = 0.67$. Whether the incorporation of iodine in the MS layer plays a critical role in promoting this value of x deserves further investigation.

3.2. Compositional analysis

We investigated the atomic composition of the single crystal and bulk samples with Energy Dispersive X-Ray Spectroscopy (EDAX) with beam energy up to 20 keV. For the measurements, the samples were adhered with carbon tape to a stainless-steel holder before placement in the vacuum chamber. The incident beam angle was 20° . Data on several single crystals revealed iodine at nominal concentrations of 15–19 at. %. For the polycrystalline samples, EDAX verified the presence of iodine at concentrations of 5–10 at. %. Example spectra are shown in Fig. 4. Qualitatively, our data suggests clean samples with no detectable bulk impurities. Small oxygen and carbon peaks are associated with surface hydrocarbons that contaminate the sample during transport through air.

3.3. Physical properties measurements

The electrical resistivity ρ versus temperature T of a $\text{Ba}_2\text{Nb}_3\text{S}_8\text{I}$ single crystal is shown in Fig. 5. The current was applied in the plane of the crystal, as illustrated in the figure. The crystallographic c direction is perpendicular to this direction. The temperature dependence is metallic with $\rho(295\text{ K})/\rho(4\text{ K}) = 13.1$. The width of the sample and the voltage lead spacing were determined by measurements under an optical microscope while the thickness was determined using an electron microscope; the resulting geometric factor was $3.3(4) \times 10^{-2}$ cm. The overall magnitude of $\rho(295\text{ K}) = 16\text{ m}\Omega\text{ cm}$ is over 9400 times larger than copper [27]. The inset of Fig. 5 reveals a transition to the superconducting state with its midpoint at $T_c = 0.57\text{ K}$; this is the temperature where ρ drops to 0.5 of its extrapolated value just above the onset to superconductivity. The transition width is 0.34 K, which was determined by taking the difference in the temperatures where ρ drops to 0.9 and 0.1 of its extrapolated value. The electrical resistivity near the superconducting transition is shown in the inset of Fig. 5 along with a partial transition in a magnetic field $H = 200\text{ Oe}$. The magnetic field was applied perpendicular to the crystal’s plane, as illustrated in the figure, which is parallel to the crystallographic c direction. The transition moves to lower temperature in magnetic field, which supports our interpretation that the transition is associated with superconductivity. A value for the slope of the critical magnetic field near T_c of $dH/dT = -412\text{ Oe/K}$ is estimated from the data of Fig. 5 (inset) based on the temperatures where ρ reaches 0.9 of its value in the normal state.

Further measurements of ρ in magnetic field (see Fig. 6) were carried out on the polycrystalline sample. It has a slightly higher $T_c = 1.36\text{ K}$, which allowed for measurements at a broader range of magnetic fields due to our limited low-temperature range. The higher T_c could be associated with differences in the nominal compositions of the single crystals and polycrystals. Magnetic fields above 10 kOe remove the complete transition in ρ within our base temperature limit of 0.4 K. The filled triangles in the main frame represent the temperatures T_x where ρ decreases to $x = 0.9$ of its value at 2 K. Similarly, filled diamonds are the values $T_{0.5}$, where ρ decreases to 0.5 of its value at 2 K and the open diamonds are the values $T_{0.1}$, where ρ drops to 0.1 of its value at 2 K. At fields below approximately 2 kOe, a noticeable upward curvature is observed in H versus T_x for $x = 0.9$. Generally, H versus T_x is linear in the low-field region, or the curvature is negative [28]. Filamentary superconductivity is likely responsible for the curvature, since it occurs in the transition region near the onset of T_c , and is absent in the $T_{0.5}$ and $T_{0.1}$ versus H data. We determined the slopes of H versus T_x for $x = 0.9$ using data from the region $H > 2\text{ kOe}$, while using all of the data in Fig. 6 for x

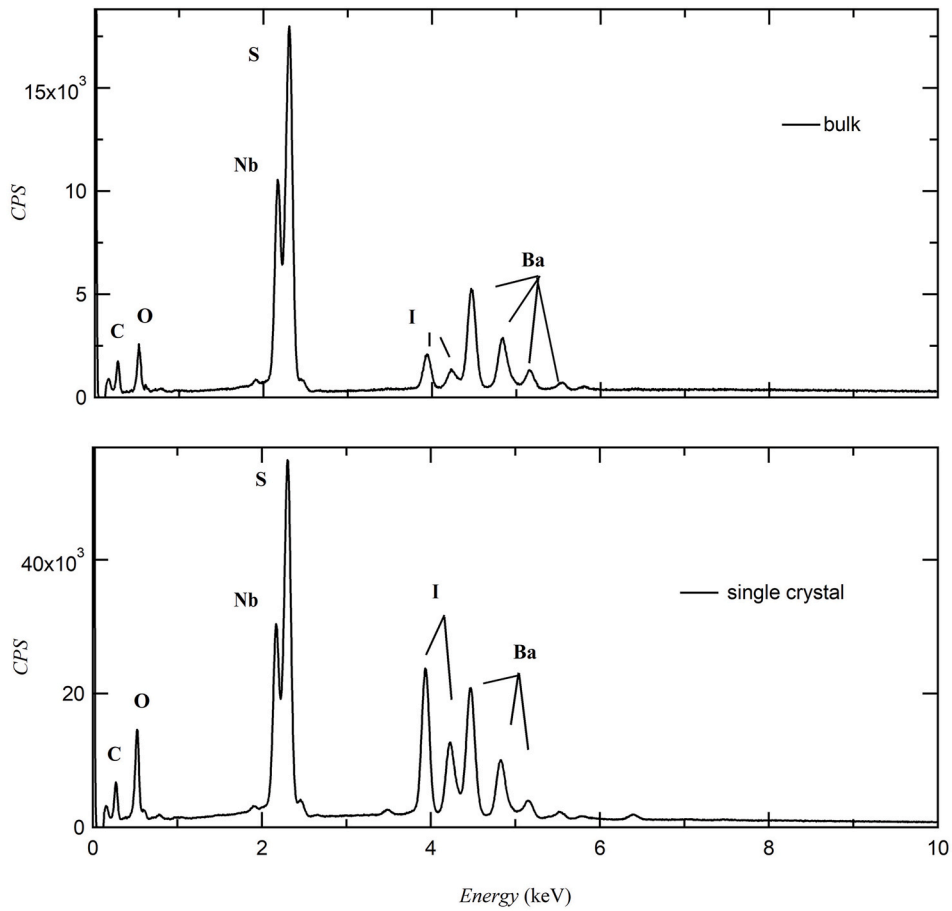


Fig. 4. Energy-dispersive x-ray spectroscopy (EDAX) plotted as intensity versus energy for Ba₂Nb₃S₈I polycrystalline (top panel) and single crystalline (bottom panel) samples.

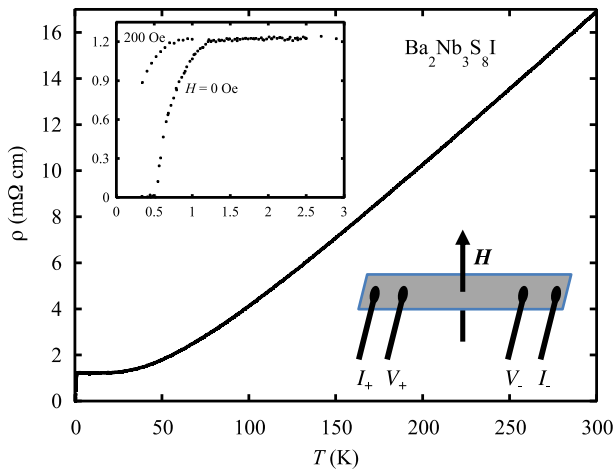


Fig. 5. Electrical resistivity versus temperature for a Ba₂Nb₃S₈I single crystal. The current was applied in the plane of the crystal and the magnetic field H was applied perpendicular to the crystal's plane, as illustrated. The magnetic field is parallel to the crystallographic c direction. Upper inset illustrates the influence of magnetic field.

= 0.5 and 0.1. Slopes of H versus T_x for $x = 0.9$ and 0.5 are determined from the region $H < 2$ kOe. The values $dH/dT_{0.9} = -6.01(52)$ kOe/K, $dH/dT_{0.5} = -1.87(78)$ kOe/K, and $dH/dT_{0.1} = -1.70(41)$ kOe/K were obtained.

The Hall effect of a Ba₂Nb₃S₈I polycrystalline specimen was

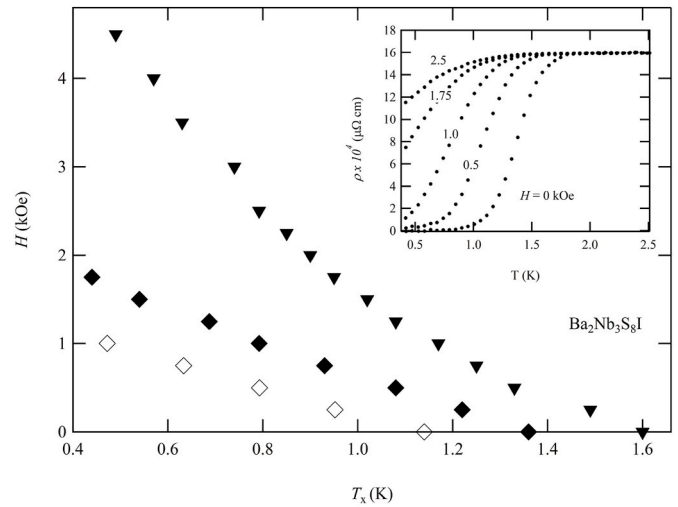


Fig. 6. The inset shows the electrical resistivity ρ versus temperature T for polycrystalline Ba₂Nb₃S₈I at magnetic fields $H = 0, 0.5, 1.0, 1.75,$ and 2.5 kOe. The temperatures T_x where the resistivity dropped to $x = 0.9, 0.5$ and 0.1 of its value at 2 K are plotted versus H in the main frame as the filled triangles, filled diamonds, and open diamonds, respectively.

measured to determine the Hall coefficient R_H and, in turn, the density, and sign of the charge carriers. The value $R_H(10 \text{ K}) = -0.0013(2) \text{ cm}^3/\text{C}$ was obtained. The negative sign indicates that the majority charge carriers in Ba₂Nb₃S₈I are electrons. The R_H value yields a charge-carrier

density of $n(10\text{ K}) = 4.8(6) \times 10^{21}\text{ cm}^{-3}$. This value was corrected for the density of the polycrystalline sample, which is only 76% of that expected for a fully-dense sample; the corrected value is $n(10\text{ K}) = 6.3(8) \times 10^{21}\text{ cm}^{-3}$. Note that if $\text{Ba}_2\text{Nb}_3\text{S}_8\text{I}$ possesses both electron and hole charge carriers, the *total* charge-carrier density would be larger. For comparison, the majority charge-carrier type and observed value of n for related compounds are listed here: BaNbS_3 (holes, $n(100\text{ K}) = 5.86(3) \times 10^{20}\text{ cm}^{-3}$) [29], BaNb_2S_5 (electrons, $n(3\text{ K}) = 2.40(2) \times 10^{21}\text{ cm}^{-3}$) [18], SrTa_2S_5 (holes, $n(5\text{ K}) = 2.75(15) \times 10^{20}\text{ cm}^{-3}$) [30,31], and BaTa_2S_5 (holes, $n(6.25\text{ K}) = 6.57(2) \times 10^{20}\text{ cm}^{-3}$) [31,32]. Our observed magnitude of n for $\text{Ba}_2\text{Nb}_3\text{S}_8\text{I}$ is comparable to these. In the case of the intercalated compound $\text{Fe}_{0.25}\text{NbS}_2$, hole-like carriers with $n = 7 \times 10^{21}$ are observed near room temperature, but the carrier majority changes to electrons between 110 K and 40 K, then back to holes below 40 K [10]. Similar behavior, and magnitude of n near 295 K, is observed in $\text{Mn}_{0.33}\text{NbS}_2$ [33]. In the case of $\text{Fe}_{0.33}\text{NbS}_2$, n is hole-like, temperature insensitive, with a density similar to that of $\text{Fe}_{0.25}\text{NbS}_2$ near room temperature [10].

Magnetic susceptibility $\chi(T)$ data were collected for $2.5\text{ K} < T < 340\text{ K}$ in a magnetic field $H = 20\text{ kOe}$. The $\chi(T)$ results are shown in the main panel of Fig. 7 as χ and $1/\chi$ versus T . The data have been corrected for the diamagnetic contributions associated with the Ba^{+2} , Nb^{+4} , Nb^{+5} , S^{-2} , and I^{-} ions by adding $461.1 \times 10^{-6}\text{ cm}^3/\text{mol}$ to the data [34,35]. The average valence for Nb of +4.33 was determined by applying charge balance to the chemical formula, and the appropriate mixture of Nb^{+4} and Nb^{+5} was used [35] to estimate the diamagnetic contribution of $-13.69 \times 10^{-6}\text{ cm}^3/\text{mol}$ for the Nb ions. The data have also been corrected for Van Vleck and Pauli paramagnetism, as described in Section 4. The feature in χ near 275 K (most clearly visible in χ^{-1} , right ordinate) is consistent with an antiferromagnetic transition. Further analysis of the data is provided in Section 4 below.

Measurements of the specific heat C at constant pressure were conducted on the polycrystalline sample over the temperature range $0.6\text{ K} < T < 20\text{ K}$ in zero magnetic field. Data for the range $T < 5\text{ K}$ are shown in Fig. 8. Fitting the data to $C/T = \gamma + \beta T^2$ in the range $1.9\text{ K} < T < 5\text{ K}$ yielded $\gamma = 3.95(66)\text{ mJ/mol K}^2$ and $\beta = 5.70(5)\text{ mJ/mol K}^4$. The Debye temperature Θ_D was calculated from β with the result $\Theta_D = 69.8(2)\text{ K}$. The small magnitude of Θ_D is comparable [27] to the values of elements such as Bi, Ba, Hg, and K, and is comparable to values found for other transition-metal sulfide materials such as BaNbS_3 ($\Theta_D = 91.4(1)\text{ K}$) [29] and BaNb_2S_5 ($\Theta_D = 126.4(8)\text{ K}$) [18]. The modest magnitude of γ suggests that the conduction electrons are not strongly correlated.

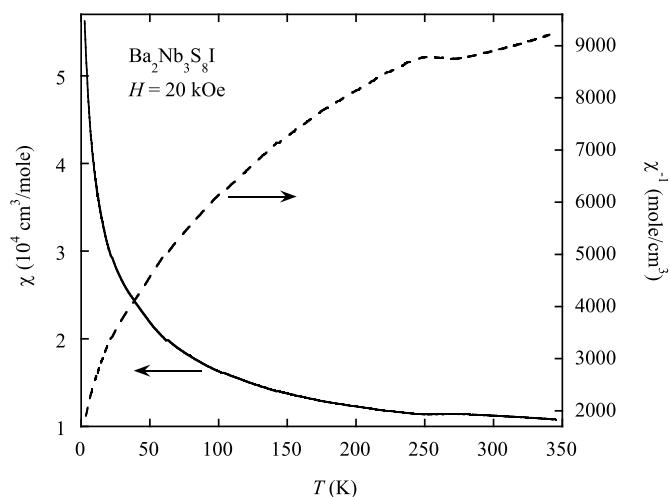


Fig. 7. Magnetic susceptibility χ versus temperature T (left ordinate, solid line) and $1/\chi$ versus T (right ordinate, dashed line) for polycrystalline $\text{Ba}_2\text{Nb}_3\text{S}_8\text{I}$ at 20 kOe. The data have been corrected for diamagnetism, Van Vleck paramagnetism, and Pauli paramagnetism (see Section 4).

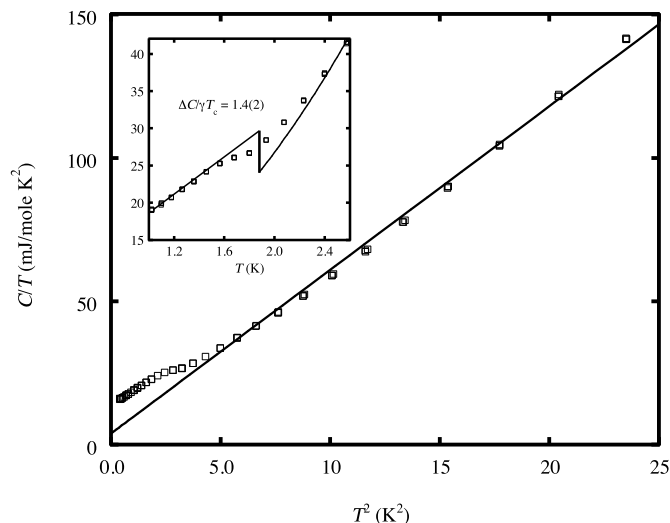


Fig. 8. Specific heat C/T versus T^2 for polycrystalline $\text{Ba}_2\text{Nb}_3\text{S}_8\text{I}$. The solid line is the fit to $C/T = \gamma + \beta T^2$. The inset illustrates the data as C/T versus T along with the entropy-conserving construction used for estimating the jump due to the superconducting phase transition (solid lines).

The C data at $H = 0$ reveal a jump at T_c that is associated with the second-order (i.e. continuous) phase transition to the superconducting state. The jump is about 0.8 K wide, and its onset appears at a slightly higher temperature than the feature in $\rho(T)$ of the same sample, which may indicate the presence of some incoherent electron pairing [36] slightly above T_c , or perhaps there exist differences in composition among pieces from the same sample. An entropy-conserving construction was used for estimating the magnitude of the jump. It is shown as the solid line in the inset of Fig. 8. Note that the line above T_c is the $C/T = \gamma + \beta T^2$ fit described above. The value $(C_s - C_n)/\gamma T_c = \Delta C/\gamma T_c = 1.4(2)$ was found. Here, C_s and C_n are the specific heats in the superconducting and normal states, respectively, in the immediate vicinity of T_c . The midpoint of the bulk phase transition to the superconducting state observed in $C(T)$ is $1.9(1)\text{ K}$, with the uncertainty related to the placement of the vertical line of the entropy-conserving construction.

4. Analysis and discussion

Observation of a transition in electrical resistivity to $\rho = 0$, the suppression of T_c by magnetic field, and a bulk-thermodynamic transition in the specific heat provide sufficient evidence of superconductivity in $\text{Ba}_2\text{Nb}_3\text{S}_8\text{I}$. The analysis that follows provides more information regarding the normal-state properties of $\text{Ba}_2\text{Nb}_3\text{S}_8\text{I}$ and the nature of its superconductivity.

The density of states $D(\epsilon_F) = 3\gamma(\pi k_B)^{-2}$ (k_B is the Boltzmann constant) can be estimated using the measured value of γ , within the free-electron model, which assumes a single band of charge carriers [27]. The value $D(\epsilon_F) = 6.3(1.1) \times 10^{42}\text{ states/J mol}$ is obtained. This leads to a Pauli paramagnetic susceptibility [27] $\chi_{\text{Pauli}} = 5.4(9) \times 10^{-5}\text{ cm}^3/\text{mol}$.

The obtained $D(\epsilon_F)$ can be used to estimate the Fermi energy ϵ_F using $D(\epsilon_F) = 3n/2\epsilon_F$ leading to $\epsilon_F = 12.3(1.8)\text{ eV}$. An estimate for ϵ_F was also attempted using [27] $\epsilon_F = (\hbar^2/2m_e)(3\pi^2n)^{2/3}$, where \hbar is Planck's constant divided by 2π and m_e is the electron's rest mass. This led to $\epsilon_F = 1.2(1)\text{ eV}$, and in turn, $\gamma = 39(4)\text{ mJ/mol K}^2$, which is nearly ten times larger than the observed value. Thus, we conclude that $\epsilon_F = 12.3(1.8)\text{ eV}$ is the more reliable value. Using it, the Fermi velocity is estimated at $v_F = 2.1(2) \times 10^6\text{ m/s}$. The charge-carrier relaxation time in the normal state, just above T_c , $\tau = m_e/(e^2n\rho) = 4.7(5) \times 10^{-15}\text{ s}$, was obtained, leading to the estimated mean-free path $\ell = v_F\tau = 99(20)\text{ \AA}$. The $\rho(2\text{K})$ measured on the single crystal (see Fig. 5) was used here, since the value

from the polycrystalline sample is about 130 times larger, and most certainly dominated by intergranular resistance. Finally, the intrinsic coherence length was estimated using the BCS formula, $\xi_0 = 0.18\hbar v_F / k_B T_c$; $\xi_0 = 4.8(5) \mu\text{m}$ was obtained, which neglects any effects of anisotropy.

Before further analysis, the $\chi(T)$ data were corrected for core diamagnetism, χ_{Pauli} , and χ_{VV} . A value of $\chi_{\text{VV}} = 3.75 \times 10^{-4} \text{ cm}^3/\text{mol}$ was estimated for $\text{Ba}_2\text{Nb}_3\text{S}_8\text{I}$ by averaging the χ_{VV} values per Nb ion obtained for BaNbS_3 and BaNb_2S_5 [18,29]. This estimate compares well with values reported for SrTa_2B_5 , BaTa_2B_5 [30,32], and Nb and Ta cluster compounds [37]. After making these corrections, the data were fitted to the Curie-Weiss formula ($\chi = C_{\text{CW}}/(T - \Theta_{\text{CW}})$) in two regions. The region $280 \text{ K} < T < 330 \text{ K}$ yielded a Curie-Weiss parameter $C_{\text{CW}} = 0.148(1) \text{ cm}^3\text{K}/\text{mol}$, which in turn yields an effective number of Bohr magnetons $p_{\text{eff}} = 0.629(2)$. The fitting also yields a Curie-Weiss temperature $\Theta_{\text{CW}} = -1020(5) \text{ K}$. Three other regions were fitted. The region $150 \text{ K} < T < 200 \text{ K}$ yielded: $C_{\text{CW}} = 56.7(2) \times 10^{-3}(1) \text{ cm}^3\text{K}/\text{mol}$ and $p_{\text{eff}} = 0.389(1)$, with $\Theta_{\text{CW}} = -263(2) \text{ K}$. The region 70 K yielded: $70 \text{ K} < T < 100 \text{ K}$, $C_{\text{CW}} = 34.3(1) \times 10^{-3}(1) \text{ cm}^3\text{K}/\text{mol}$ and $p_{\text{eff}} = 0.302(1)$, with $\Theta_{\text{CW}} = -111(1) \text{ K}$. Finally, the region $2.5 \text{ K} < T < 8 \text{ K}$ yielded: $C_{\text{CW}} = 8.62(8) \times 10^{-3}(1) \text{ cm}^3\text{K}/\text{mol}$ and $p_{\text{eff}} = 0.152(1)$, with $\Theta_{\text{CW}} = -12.9(2) \text{ K}$.

Let's first consider the observed value of p_{eff} above 300 K. The expected value of p_{eff} for Nb^{+4} , a $4d^1$ configuration, is 1.55 if the angular momentum is not quenched, or 1.73 if the angular momentum is quenched [27] and Nb^{+5} , a $4d^0$ state, would be non-magnetic. According to charge balance, 67% of the Nb ions would be Nb^{+4} , indicating that $p_{\text{eff}} \sim 1$ might be expected. The sizable deviation from this suggests that the $4d^1$ electron is strongly itinerant, however, a localized magnetic moment is clearly present. For the region below the transition at 275 K, the value of p_{eff} becomes smaller with decreasing temperature. Thus, the magnetic moment is reduced as a result of the transition in $\chi(T)$ near 275 K, reflecting a significant loss of the paramagnetism. We postulate that it is the result of antiferromagnetic order due to the magnetic moments gradually assuming a fully ordered state as T is reduced. The value of p_{eff} observed below 8 K can probably be attributed to disorder or impurities, both of which are expected in a polycrystalline specimen. In addition, the strongly negative value of $\Theta_{\text{CW}} = -1020(5) \text{ K}$ in the region $280 \text{ K} < T < 330 \text{ K}$ indicates antiferromagnetic correlations, in further support of an antiferromagnetic state below 275 K. For the related compounds that we have studied, BaNbS_3 , BaNb_2S_5 , BaTa_2S_5 , and SrTa_2S_5 [18,29,30,32], the transition metal possesses only Pauli and Van Vleck paramagnetism. Thus, the sizable magnetic moment detected above 275 K of $p_{\text{eff}} = 0.629(2)$ in $\text{Ba}_2\text{Nb}_3\text{S}_8\text{I}$ is unexpected. Furthermore, antiferromagnetic order would be particularly surprising in a compound that exhibits superconductivity. Neutron diffraction measurement would be useful to determine whether or not this compound does indeed order antiferromagnetically below 275 K.

The jump in the specific heat for a conventional superconductor is expected [28,38] to be $\Delta C/\gamma T_c = 1.43$. Our observation of 1.4(2), as shown in Fig. 8, agrees well with this value. The presence of a jump at T_c and the magnitude of the jump in the polycrystalline $\text{Ba}_2\text{Nb}_3\text{S}_8\text{I}$ sample illustrates that it is a bulk superconductor. As a corollary, the single crystals can safely be assumed to possess bulk superconductivity. The $C(T)$ data were plotted as $\ln(C/\gamma T_c)$ versus T_c/T to investigate the presence of an energy gap below T_c , and to compare to the prediction from BCS theory

$$C = A\gamma T_c e^{-BT_c/T}. \quad (1)$$

Good linear behavior was observed only in the region $1 < T_c/T < 1.61$. The fit for this region is shown in Fig. 9 as the dashed line; it yielded the values $A = 3.15(1)$ and $B = 1.23(1)$, using $T_c = 1.9(1) \text{ K}$. BCS theory [38] predicts $A = 8.5$ and $B = 1.44$. Our value of B is close to this. The obtained value for A is much smaller than the BCS result. Measurements on related compounds [18,29] also reveal poor agreement of

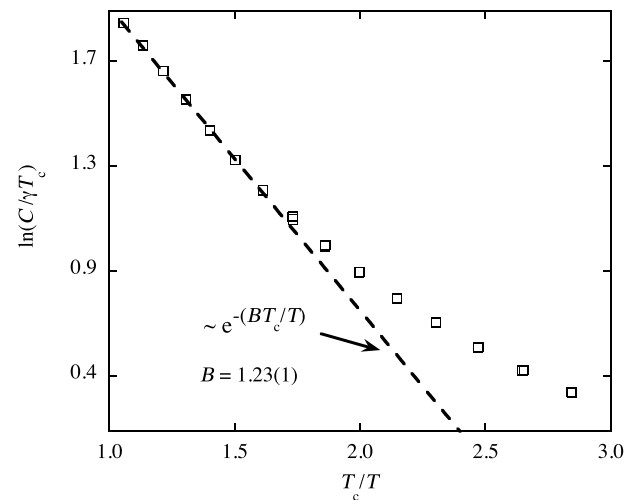


Fig. 9. Plot of $\ln(C/\gamma T_c)$ versus T_c/T for $\text{Ba}_2\text{Nb}_3\text{S}_8\text{I}$ below T_c . The dashed line is a fit to the data for the region $1 < T_c/T < 1.61$, using the prediction from BCS theory $C = A\gamma T_c e^{-BT_c/T}$.

A with the BCS value; the reason for the discrepancy is unclear. The energy gap E_g is given by Ref. [27] $E_g = 2BT_c$, which yields $E_g = 4.7(2) \text{ K}$ or $0.405(17) \text{ meV}$. This is smaller than the value expected from BCS theory [28,38] of $E_g = 3.528 k_B T_c = 0.58 \text{ meV}$. The strong curvature in the data for $T_c/T > 1.61$ suggests the presence of a second energy gap, which is known for some superconductors, such as MgB_2 [39]. A fit to the region $2 < T_c/T < 3$ gives a value of $B \approx 0.5$ for an energy gap of 1.9 K (0.23 meV).

The critical magnetic field data in Fig. 6 were used to estimate the coherence length as $T \rightarrow 0$ using the equation [28].

$$\xi(T) = \frac{\Phi_0}{2\sqrt{2}\pi H_{0.5}(T)\lambda_{\text{eff}}(T)}; \quad (2)$$

$\Phi_0 = 2.07 \times 10^{-7} \text{ Oe cm}^2$ is the magnetic flux quantum. Note that $\lambda_L(0) = \sqrt{mc^2/4\pi e^2}$ (cgs), where e is the electron charge, and $\lambda_{\text{eff}}(T) = \lambda_L(0)(1 - (T/T_c)^4)^{-1/2}$. The value $\lambda_L(0) = 6700(400) \text{ nm}$, was obtained. We determined $H_{0.5}(0 \text{ K}) = 1.02 \text{ kOe}$ by extrapolating the $H_{0.5}(T_x)$ curve to $T = 0$. The final result is $\xi(0 \text{ K}) = 3400(200) \text{ nm}$. The broadening of the $\rho(T)$ transitions with field suggests that the superconductivity of $\text{Ba}_2\text{Nb}_3\text{S}_8\text{I}$ is strongly anisotropic. To characterize the impact of this on ξ , $H_{0.1}(0.5 \text{ K})$ and an extrapolated value of $H_{0.9}(0.5 \text{ K})$ with Eq. (2) were used to estimate $\xi(0.5 \text{ K})$ yielding values of $3900(300) \text{ nm}$ and $770(40) \text{ nm}$, respectively. The Ginzburg-Landau parameter $\kappa = \lambda_{\text{eff}}/\xi > 1/\sqrt{2}$ for all estimated values of ξ , indicating that $\text{Ba}_2\text{Nb}_3\text{S}_8\text{I}$ is a Type II superconductor. Note that the resulting values of ξ are quite large, and on par with many elements [27]. However, they are comparable in magnitude to the intrinsic coherence length ξ_0 .

5. Conclusions

The compound $\text{Ba}_2\text{Nb}_3\text{S}_8\text{I}$ is reported for the first time. It was grown accidentally in single crystal form when attempting to grow BaNb_2S_5 in an iodine-vapor-transport medium. The incorporation of iodine into the resultant crystals is an important aspect of this work, suggesting that the growth of other compounds in an iodine-vapor-transport medium may result in iodine incorporation into them as well. The crystal structure was determined to be trigonal with space group $P31c$ and lattice parameters $a = b = 10.0156(5) \text{ \AA}$ and $c = 25.1414(15) \text{ \AA}$. It can be viewed as an intercalation compound with salt-like BaS layers containing I, intercalated between each NbS_2 layer. Intercalation of I^- , with its large radius of 220 pm [26], stabilizes a distortion of the BaS layer from cubic symmetry. This permits the incorporation of the distorted rocksalt-like

BaS layer between the NbS₆ trigonal prisms of the NbS₂ layers. The Ba₂Nb₃S₈I single crystals are superconducting with $T_c \sim 0.57$ K. Due to the small size of the single crystals, most of the physical properties measurements were executed on polycrystalline samples. Ba₂Nb₃S₈I is a bulk type-II superconductor with $T_c \sim 1.36$ K, in bulk polycrystalline form. The higher T_c is likely associated with differences in the nominal compositions. Magnetic susceptibility measurements reveal a magnetic moment attributed to the Nb ion with an effective number of Bohr magnetons $\mu_{\text{eff}} = 0.629(2)$. Ba₂Nb₃S₈I appears to be antiferromagnetic below 275 K. This needs confirmation with neutron diffraction, since the coexistence of antiferromagnetism and superconductivity would be very surprising.

Author roles

Michael G. Smith: Directed project, synthesized polycrystal specimens, acquired and analyzed powder x-ray diffraction data, and participated in writing manuscript.

Qisheng Lin: Conducted single-crystal x-ray diffraction analysis, structure identification, and participated in writing manuscript.

S. M. Benjamin: Conducted low-temperature measurements and data analysis.

Mitchell T. Baker: Grew and characterized single crystals, conducted low-temperature physical properties measurements, conducted x-ray diffraction measurements and data analysis of powdered single crystals, wrote crystal growth portion of manuscript.

John J. Neumeier: Assisted in project direction, conducted low-temperature physical properties measurements, wrote majority of manuscript.

Declaration of competing interest

The authors declare that they have no known competing financial interests or personal relationships that could have appeared to influence the work reported in this paper.

Acknowledgements

Work at Montana State University was conducted with financial support from the US Department of Energy (DOE), Office of Science, Basic Energy Sciences (BES) under Award No. DE-SC0016156; this includes the growth, characterization, physical properties measurements, and data analysis, which were conducted by MGS, SMB, MTB, and JJN. Work performed at Ames Laboratory was supported by the U.S. Department of Energy (DOE), Office of Science, Basic Energy Sciences, Materials Science and Engineering Division; this includes the crystal structure determination, which was conducted by QL. Ames Laboratory is operated for the U.S. DOE by Iowa State University under contract DE-AC02-07CH11358.

Appendix A. Supplementary data

Supplementary data to this article can be found online at <https://doi.org/10.1016/j.jpcs.2021.110135>.

References

- X.-C. Liu, S. Zhao, X. Sung, L. Deng, X. Zhou, Y. Hu, W.-X. Wang, C.-W. Chu, J. Li, J. Wu, F.-S. Ke, P.M. Ajayan, Spontaneous self-intercalation of copper atoms into transition metal dichalcogenides, *Sci. Adv.* 6 (2020), eaay4092.
- G. Wieggers, Misfit layer compounds: structures and physical properties, *Prog. Solid State Chem.* 24 (1–2) (1996) 1–139.
- B.W. Eichorn, Ternary transition metal sulfides, in: K.D. Karlin (Ed.), *Progress in Inorganic Chemistry*, vol. 42, Wiley and Sons, Inc., New York, NY, USA, 1994, pp. 139–237.
- L.S. Panchakarla, G. Radovsky, L. Houben, R. Popovitz-Biro, R.E. Dunin-Borkowski, R. Tenne, Nanotubes from misfit layered compounds: a new family of materials with low dimensionality, *J. Phys. Chem. Lett.* 5 (21) (2014) 3724–3736.
- F. Jellinek, G. Brauer, H. Müller, Molybdenum and niobium sulphides, *Nature* 185 (4710) (1960) 376–377.
- W.G. Fisher, M. Sienko, Stoichiometry, structure, and physical properties of niobium disulfide, *Inorg. Chem.* 19 (1) (1980) 39–43.
- H.V. van Maaren, G.M. Schaeffer, Superconductivity in group VA dichalcogenides, *Phys. Lett.* 20 (1966), 131–131.
- M. Chhowalla, H.S. Shin, G. Eda, L.-J. Li, K.P. Loh, H. Zhang, The chemistry of two-dimensional layered transition metal dichalcogenide nanosheets, *Nat. Chem.* 5 (4) (2013) 263.
- F. Hulliger, E. Pobitschka, On the magnetic behavior of new 2H NbS₂-type derivatives, *J. Solid State Chem.* 1 (2) (1970) 117–119.
- O. Gorochov, A. Le Blanc-Soreau, J. Rouxel, P. Imbert, G. Jehanno, Transport properties, magnetic susceptibility and Mössbauer spectroscopy of Fe_{0.25}NbS₂ and Fe_{0.33}NbS₂, *Philos. Mag. A B* 43 (4) (1981) 621–634.
- T. Terashima, N. Kojima, Electrical transport properties of incommensurate layer compounds (ReS)_xNbS₂ (Re = rare-earth metals; x = 1.2, 0.6), *J. Phys. Soc. Jpn.* 63 (2) (1994) 658–673.
- P. Jood, M. Ohta, Hierarchical architecture for layered thermoelectric sulfides and chalcogenides, *Materials* 8 (3) (2015) 1124–1149.
- P. Jood, M. Ohta, H. Nishiye, A. Yamamoto, O.I. Lebedev, D. Berthebaud, K. Suekuni, M. Kunii, Microstructural control and thermoelectric properties of misfit layered sulfides (LaS)_(1+m)TS₂ (T = Cr, Nb): the natural superlattice systems, *Chem. Mater.* 26 (8) (2014) 2684–2692.
- A. Meerschaut, P. Rabu, J. Rouxel, Preparation and characterization of new mixed sandwiched layered compounds Ln₃₂Nb₂₈S₈₈ (Ln = La, Ce), *J. Solid State Chem.* 78 (1) (1989) 35–45.
- D. Reefman, J. Baak, H. Brom, G. Wieggers, Superconductivity in misfit layer compounds (MS)_nTS₂, *Solid State Commun.* 75 (1) (1990) 47–51.
- O. Pena, P. Rabu, A. Meerschaut, Magnetic properties of rare-earth-based misfit layered materials of formula (LnS)_nNbS₂ (Ln identical to lanthanides, Y), *J. Phys. Condens. Matter* 3 (49) (1991) 9929.
- T. Terashima, N. Kojima, Magnetic properties of incommensurate layer compounds, (CeS)_{1.2}NbS₂ and (CeS)_{0.6}NbS₂, *J. Phys. Soc. Jpn.* 61 (9) (1992) 3303–3312.
- M.G. Smith, J.J. Neumeier, Observation of superconductivity in BaNb₂S₅, *Physica C: Superconduct. Appl.* 549 (2018) 88–92, <https://doi.org/10.1016/j.physc.2018.03.004>. <http://www.sciencedirect.com/science/article/pii/S0921453418300455>.
- R. Woods-Robinson, Y. Han, H. Zhang, T. Ablekim, I. Khan, K.A. Persson, A. Zakutayev, Wide band gap chalcogenide semiconductors, pMID: 32250103. arXiv:10.1021/acs.chemrev.9b00600, *Chem. Rev.* 120 (9) (2020) 4007–4055, <https://doi.org/10.1021/acs.chemrev.9b00600>, <https://doi.org/10.1021/acs.chemrev.9b00600>.
- M. VanHorne, F. Comhaire, Epidemiological study of the effects of carbon disulfide on male sexuality and reproduction, *Arch. Environ. Health* 49 (4) (1994) 273–278.
- Saint Plus Version 8.30, Tech. Rep., Bruker AXS Inc., Madison, Wisconsin, USA, 2013.
- V.M. Petricek, M. Dusek, L. Palatinus, Tech. Rep. in: Jana2006. The Crystallographic Computing System, Institute of Physics, Praha, Czech Republic, 2006.
- L. Palatinus, G. Chapuis, Superflip - a computer program for the solution of crystal structures by charge flipping in arbitrary dimensions, *J. Appl. Crystallogr.* 40 (2007) 786–790.
- A.L. Spek, Platon, *J. Appl. Crystallogr.* 36 (2003) 7–13.
- G.S. Smith, R.L. Snyder, FN: a criterion for rating powder diffraction patterns and evaluating the reliability of powder-pattern indexing, *J. Appl. Crystallogr.* 12 (1979) 60–65.
- R.D. Shannon, Revised effective ionic radii and systematic studies of interatomic distances in halides and chalcogenides, *Acta Crystallogr. A* 32 (1976) 751–767.
- C. Kittel, *Introduction to Solid State Physics*, John Wiley, New York, NY, 1996.
- M. Tinkham, *Introduction to Superconductivity*, Robert E. Krieger, Malabar, FL, USA, 1985.
- J.J. Neumeier, M.G. Smith, Superconductivity in quasi-one-dimensional BaNbS₃, *Physica C* 542 (2017) 1–5.
- A.K. Drenner, S.M. Benjamin, M.G. Smith, J.J. Neumeier, Physical properties and superconductivity of SrTa₂S₅, *Physica C: Superconduct. Appl.* 556 (2019) 19–23, <https://doi.org/10.1016/j.physc.2018.11.006>. <http://www.sciencedirect.com/science/article/pii/S0921453418303575>.
- H. Nozaki, M. Saeki, M. Onoda, Superconducting and normal state properties of barium tantalum sulfide, *J. Solid State Chem.* 116 (1995) 392–399.
- A.K. Drenner, S.M. Benjamin, M.G. Smith, J.J. Neumeier, Physical properties and superconductivity of BaTa₂S₅, *Physica C: Superconduct. Appl.* 566 (2019) 1353522, <https://doi.org/10.1016/j.physc.2019.1353522>. <http://www.sciencedirect.com/science/article/pii/S092145341930231X>.
- R.H. Friend, A.R. Beal, A.D. Yoffe, Electrical and magnetic properties of some first row transition metal intercalates of niobium disulphide, arXiv:10.1080/14786437708232952, *Phil. Mag.: A Journal of Theoretical Experimental and Applied Physics* 35 (5) (1977) 1269–1287, <https://doi.org/10.1080/14786437708232952>, <https://doi.org/10.1080/14786437708232952>.
- R.R. Gupta, Diamagnetic Susceptibility of Diamagnetic and Paramagnetic Ions, *Landolt-Börnstein, New Series II/16*, Springer-Verlag, Heidelberg, 1986, p. 402. Ch. 7.
- E. König, G. König, Selected diamagnetic ionic susceptibilities, Pascal constants, and one-electron spin-orbit coupling constants, in: K.-H. Hellwege, A.M. Hellwege (Eds.), *Landolt-Börnstein - Group II Molecules and Radicals Volume 8, Magnetic*

- Properties of Coordination and Organometallic Transition Metal Compounds, vol. 8, Springer-Verlag, Berlin, 1976, pp. 27–29.
- [36] D. Das, S. Doniach, Bose metal: gauge-field fluctuations and scaling for field-tuned quantum phase transitions, *Phys. Rev. B* 64 (13) (2001) 134511, <https://doi.org/10.1103/PhysRevB.64.134511>.
- [37] J.G. Converse, R.E. McCarley, Chemistry of polynuclear metal halides. vi. magnetic susceptibility studies of some niobium and tantalum halide cluster derivatives, *Inorg. Chem.* 9 (6) (1970) 1361–1366.
- [38] J. Bardeen, L.N. Cooper, J.R. Schrieffer, Theory of superconductivity, *Phys. Rev.* 108 (5) (1957) 1175–1204.
- [39] F. Bouquet, R.A. Fisher, N.E. Phillips, D.G. Hinks, J.D. Jorgensen, Specific heat of Mg^{11}B_2 : evidence for a second energy gap, *Phys. Rev. Lett.* 87 (2001), 047001, <https://doi.org/10.1103/PhysRevLett.87.047001>. <https://link.aps.org/doi/10.1103/PhysRevLett.87.047001>.